

- sized and quantified as described in (5).
8. J. S. Stampler *et al.*, data not shown.
  9. SNO-RBCs ( $\sim 1 \mu\text{M}$ ) caused  $32.5 \pm 1.2\%$  relaxation that lasted  $14.5 \pm 0.7$  min in 95%  $\text{O}_2$  versus  $61 \pm 10\%$  relaxation that lasted  $23 \pm 2$  min in  $<1\%$   $\text{O}_2$  ( $n = 3$  to  $4$ ;  $P < 0.05$ ). SNO-RBCs ( $\sim 0.1 \mu\text{M}$ ) produced small relaxations in  $<1\%$   $\text{O}_2$  and small contractions in 95%  $\text{O}_2$ . In contrast, RBCs containing no SNO-Hb produced small contractions (less than those of cell-free Hb) that were potentiated by hypoxia ( $13 \pm 2.0\%$  in 95%  $\text{O}_2$  versus  $25 \pm 5\%$  in  $<1\%$   $\text{O}_2$ ;  $P < 0.05$ ).
  10. Protein modeling was done with SYBYL software from TRIPOS Inc. (St. Louis, MO). Hemoglobin coordinates came from the Brookhaven Protein Data Bank (PDB): In oxy Hb, 1HCO and other PDB coordinate files; in deoxy Hb, 3HHB and other PDB files. NO was modeled onto oxy Hb and deoxy Hb with the use of the bond distances and angles recorded in S. Oae and K. Shinhama [*Org. Prep. Proc. Int.* **15**, 165 (1983)] with rotational freedom about the  $\text{C}\alpha\text{-C}\beta$ ,  $\text{C}\beta$ ,  $\text{C}\beta\text{-S}\gamma$ ,  $\text{S}\gamma\text{-N}\delta$  bonds. Figures were prepared with the program VIEW (L. Bergman, University of North Carolina).
  11. Adult Sprague-Dawley rats (290 to 350 g) were anesthetized with sodium pentobarbital, intubated, and ventilated with a respirator to maintain the arterial  $\text{CO}_2$  pressure at 35 to 45 mmHg. Drugs were infused through the femoral vein, and blood pressure was monitored via the femoral artery as described in (5). Blood gas tensions and pH were measured periodically; the blood was replaced with three volumes of 0.9% saline. The tissue  $\text{PO}_2$  was measured with platinum microelectrodes (50  $\mu\text{m}$  outer diameter, coated with Nafion) implanted stereotaxically in the right and left hippocampus (AP,  $-3.4$  mm; ML,  $+2.2$  mm), caudate putamen nucleus (CPN), and substantia nigra (SN) (see coordinates below) as described in C. A. Piantadosi *et al.*, *Free Rad. Biol. Med.* **22**, 725 (1997). The  $\text{PO}_2$  electrodes were polarized to  $-0.65$  V against an Ag/AgCl reference, and the current was measured with a low-impedance nanoampere meter. Arterial  $\text{PO}_2$  was adjusted by changing the inspired  $\text{O}_2$  concentration and atmospheric pressure. Hydrogen ( $\text{H}_2$ )-sensitive platinum microelectrodes were implanted stereotaxically in the SN (AP,  $-5.3$  mm; ML,  $-2.4$  mm to the bregma, depth 3.2 mm), CPN (AP,  $+0.8$  mm; ML,  $-2.5$  mm, depth 5.2 mm), and parietal cortex, for measurement of regional blood flow. The microelectrodes were insulated with epoxy, with the exception of the Nafion-coated tip (1 mm). The electrodes were polarized to 400 mV against a reference electrode, and the current was measured with a low-impedance nanoampere meter during and after the inhalation of hydrogen gas (2.5%) for 1 min. The  $\text{H}_2$ -clearance curves and  $\text{O}_2$  tracings were recorded with PC WINDAQ (software, DI-200 AC; DATA Q Instruments, OH). Cerebral blood flow was calculated with the initial slope method [W. D. Heiss and H. Traupe, *Stroke* **12**, 161 (1981); W. Young, *ibid.* **11**, 552 (1980)]. Regional blood flow was monitored for 30 min before and after drug administration (time 0).
  12. P. M. Tibbles and J. S. Edelsberg, *N. Engl. J. Med.* **334**, 1642 (1996).
  13. Approximately  $0.1 \mu\text{M}$  SNO-RBCs lowered blood pressure by  $7 \pm 1$  mmHg and  $\sim 0.5 \mu\text{M}$  SNO-RBCs lowered blood pressure by  $16 \pm 2$  mmHg ( $n = 8$ ;  $P < 0.001$  versus baseline).
  14. M. W. Dewhirst, T. W. Secomb, E. T. Ong, R. Hsu, J. F. Gross, *Cancer Res.* **54**, 3333 (1994); H. Kerger, I. Torres Filho, M. Rivas, R. Winslow, M. Intaglietta, *Am. J. Physiol.* **268**, H802 (1995).
  15. K. H. Park, L. E. Rubin, S. S. Gross, R. Levi, *Circ. Res.* **71**, 992 (1992); V. Hampl, S. L. Archer, D. P. Nelson, E. K. Weir, *J. Appl. Physiol.* **75**, 1748 (1993).
  16. M. Casadevall *et al.*, *Gastroenterology* **110**, 1156 (1996); S.-M. Kasper *et al.*, *Anesth. Analg.* **83**, 921 (1996); J. S. Stampler, *Nature* **380**, 108 (1996); M. G. Persson, L. E. Gustafsson, N. P. Wiklund, P. Hedqvist, S. Moncada, *Br. J. Pharmacol.* **100**, 463 (1990); D. Mitchell and K. Tyml, *Am. J. Physiol.* **270** (*Heart Circ. Physiol.* **39**), H1696 (1996); C. E. King *et al.*, *J. Appl. Physiol.* **76**, 1166 (1994).
  17. We are indebted to M. Dewhirst for his insight. J.S.S.

is a Pew scholar in the biomedical sciences and the recipient of grants from the National Heart, Lung, and Blood Institute (NHLBI) (HL 52529 and

HR59130). C.A.P. is funded by the NHLBI.

17 January 1997; accepted 2 May 1997

## In Vivo Endoscopic Optical Biopsy with Optical Coherence Tomography

Guillermo J. Tearney, Mark E. Brezinski,\* Brett E. Bouma, Stephen A. Boppart, Costas Pitris, James F. Southern, James G. Fujimoto

Current medical imaging technologies allow visualization of tissue anatomy in the human body at resolutions ranging from 100 micrometers to 1 millimeter. These technologies are generally not sensitive enough to detect early-stage tissue abnormalities associated with diseases such as cancer and atherosclerosis, which require micrometer-scale resolution. Here, optical coherence tomography was adapted to allow high-speed visualization of tissue in a living animal with a catheter-endoscope 1 millimeter in diameter. This method, referred to as "optical biopsy," was used to obtain cross-sectional images of the rabbit gastrointestinal and respiratory tracts at 10-micrometer resolution.

Medical imaging technology has advanced over the last 20 years to provide physicians with indispensable information on the macroscopic anatomy of patients. Imaging techniques such as conventional x-ray radiography, magnetic resonance imaging, computed tomography, and ultrasonography have allowed the noninvasive investigation of large-scale structures in the human body with resolutions ranging from 100  $\mu\text{m}$  to 1 mm. However, this resolution is insufficient for the identification of many important pathologies, such as early neoplastic changes or coronary atherosclerotic plaques predisposed to rupture. Identification of these abnormalities requires technologies that resolve clinically relevant tissue microstructure in the range of conventional biopsy.

Optical coherence tomography (OCT) is an optical imaging technique that allows high-resolution cross-sectional imaging of tissue microstructure (1). OCT is analogous to ultrasound imaging except that infrared light waves rather than acoustic waves are used. An optical beam is focused into the tissue, and the echo time delay of light reflected from internal microstructure at different depths is measured by interferometry. Image information is obtained by per-

forming repeated axial measurements at different transverse positions as the optical beam is scanned across the tissue. The resulting data constitute a two-dimensional map of the backscattering or reflectance from internal architectural morphology and cellular structures in the tissue.

OCT is attractive for clinical imaging for three reasons. (i) The typical OCT image has an axial resolution of 10  $\mu\text{m}$ , up to 10 times higher than any clinically available diagnostic imaging modality. (ii) Because OCT systems can be constructed with fiber optical components used in telecommunications, they are relatively inexpensive and portable. (iii) Fiber optic systems can be incorporated into catheters or endoscopes, allowing high-resolution images of internal organ microstructure.

Initially, OCT was applied to imaging the transparent tissue of the eye (2, 3). Clinical studies have shown that OCT provides high-resolution cross-sectional images of a wide range of retinal macular diseases (4, 5). Recently, imaging to depths of 2 to 3 mm in nontransparent tissue was achieved by use of longer wavelengths in the near infrared (1, 6–9). The identification of in vitro pathology has been verified in tissue from the cardiovascular system and gastrointestinal tract (8, 10).

Here we demonstrate in vivo endoscope-based OCT imaging of the gastrointestinal and respiratory tracts of a rabbit at an axial resolution of 10  $\mu\text{m}$ . To achieve this resolution, we constructed an OCT system that uses a light source with appropriate power and wavelength characteristics, a high-speed optical delay line based on femtosecond pulse shaping, and a second-generation

G. J. Tearney, B. E. Bouma, S. A. Boppart, C. Pitris, J. G. Fujimoto, Department of Electrical Engineering and Computer Science and Research Laboratory of Electronics, Building 36-357, Massachusetts Institute of Technology, 77 Massachusetts Avenue, Cambridge, MA 02139, USA. M. E. Brezinski, Cardiac Unit, Massachusetts General Hospital (Harvard Medical School), Knight Catheterization Laboratory, Fruit Street, Boston, MA 02114, USA. J. F. Southern, Department of Pathology, Sinai Samaritan Hospital, Milwaukee, WI 53233, USA.

\*To whom correspondence should be addressed at Building 36-357, Massachusetts Institute of Technology, 77 Massachusetts Avenue, Cambridge, MA 02139, USA. E-mail: mebrezin@mit.edu

OCT catheter-endoscope.

A schematic of the endoscopic OCT imaging system is shown in Fig. 1A. A low-coherence length light source is coupled into a fiber optic Michelson interferometer. The catheter-endoscope is in one arm of the interferometer and a scanning temporal delay is in the other arm. Interference is observed only when the path lengths of the interferometer arms are matched to within the coherence length of the source. The interference signal is detected and demodulated to yield the echo delay of backscattered light from the tissue. Images are acquired by scanning the beam position on the tissue and displaying the resulting data in image form.

To achieve high resolution with rapid image acquisition rates, we constructed a short-pulse, Kerr-lens modelocked Cr<sup>4+</sup>:forsterite laser and used it as the light source for the OCT system (11, 12). This laser produced higher power and shorter coherence length light than conventional low-coherence superluminescent diode sources used in

previous systems (1, 6–9). In addition, self-phase modulation was used to broaden the optical spectrum and enhance imaging resolution. The output power was 30 mW (10 mW on the tissue) with a Gaussian full-width at half-maximum (FWHM) spectral bandwidth of 75 nm centered at 1280 nm. These parameters corresponded to a free-space axial resolution of 10 μm and a signal to noise ratio (SNR) of 110 dB.

With previous OCT systems, the optical delay in the reference arm was varied with either a linearly translating galvanometer or by stretching an optical fiber with a piezoelectric crystal (1, 13, 14). However, commercial galvanometers do not generate sufficient mechanical translation rates to allow imaging in real time (14). Piezoelectric fiber stretchers allow rapid scanning, but they suffer from high power requirements, nonlinear fringe modulation due to hysteresis, uncompensated polarization dispersion matches, and poor temperature stability. For these reasons, we designed a high-speed optical

delay line using phase control techniques originally developed for femtosecond pulse shaping (15, 16). This device can be constructed with common optical components, has modest power requirements, is repeatable, and is temperature stable.

The phase control optical delay line contained a lens-grating pair to Fourier transform the temporal profile of the low-coherence (broad-spectrum) light in the reference arm. A mirror mounted to a galvanometer, placed at the Fourier plane, allowed angular tilt to be mapped to group delay (Fig. 1A). The group delay was varied by rapidly changing the angle of the mirror mounted to the galvanometer, allowing the acquisition of 2000 axial scans per second with a total optical path length delay of ~3 mm. This method also permitted group and phase delay to be independently controlled so that the interferometric modulation frequency produced by the scanning delay could be selected commensurate with higher performance detection and data acquisition electronics.

A transverse scanning catheter-endoscope was integrated into the OCT system to facilitate high-speed in vivo intraluminal imaging of internal organs (Fig. 1, B and C). The catheter-endoscope consisted of an encased, rotating hollow cable carrying a single-mode optical fiber. The beam from the distal end of the fiber was

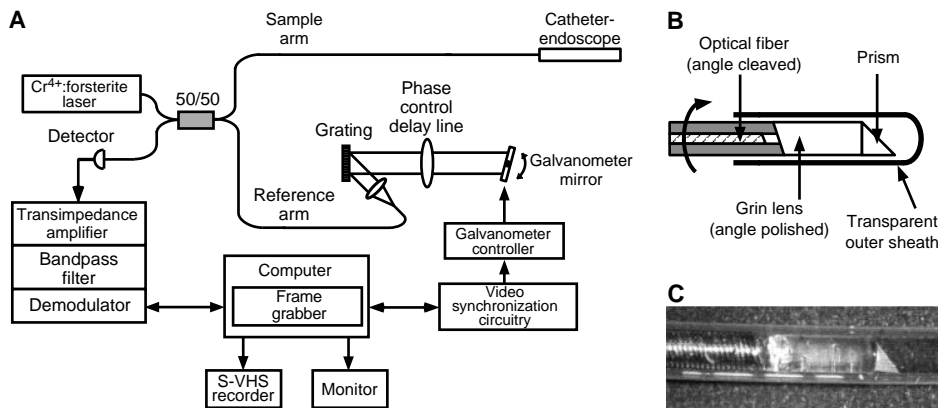


**Fig. 1.** (A) Schematic of the high-speed endoscopic OCT system. (B) Schematic of the distal optics of the second-generation OCT catheter-endoscope. The angle cleaving the optical fiber and the angle polishing the GRIN lens minimized internal reflections. (C) Photograph of the OCT catheter-endoscope distal optics.

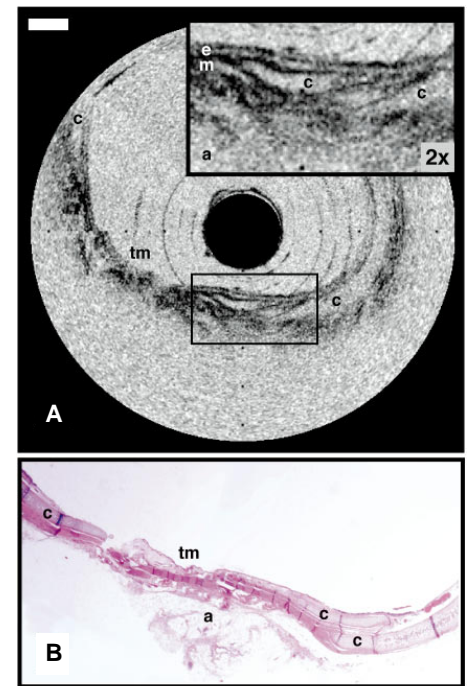


**Fig. 3.** OCT imaging of a rabbit trachea in vivo (22). (A) This image allows visualization of distinct architectural layers, including the epithelium (e), the mucosal stroma (m), cartilage (c), and adipose tissue (a). The trachealis muscle (tm) can be easily identified. (B) Corresponding histology (H&E stain). Bar, 500 μm.

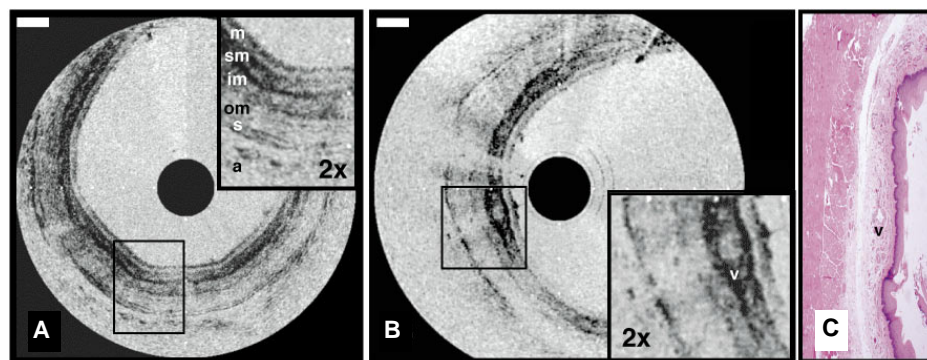


**Fig. 2.** OCT imaging of the rabbit esophagus in vivo (22). (A) This image allows visualization of the esophageal layers of the rabbit including the mucosa (m), the submucosa (sm), the inner muscular layer (im), the outer muscular layer (om), the serosa (s), and the adipose and vascular supportive tissues (a). (B) A blood vessel (v) is apparent within the submucosa of the esophagus. (C) Corresponding histology for (B) (H&E stain). Bars, 500 μm.

focused by a graded index (GRIN) lens and was directed perpendicular to the catheter axis by a micropism (Fig. 1, B and C). The distal optics were encased in a transparent housing. The beam was scanned circumferentially at four revolutions per second by rotation of the cable, fiber, and optical assembly inside the static housing. The catheter-endoscope was redesigned from an original prototype (17) to decrease its diameter, increase imaging speed, and reduce parasitic internal reflections. The confocal parameter of the distal lens was 1.9 mm, which corresponded to a focused beam diameter of 40  $\mu\text{m}$ . Power loss caused by suboptimal coupling and internal reflection within the catheter was 3 to 4 dB. The overall SNR of the OCT system with the catheter-endoscope was  $\sim 106$  dB. The catheter-endoscope had a diameter of 1 mm, which is small enough to allow imaging in a human coronary artery or access through the flush port of a standard endoscope.

OCT images of the *in vivo* rabbit esophagus allowed visualization of all layers of the esophageal wall (Fig. 2, A and B). For example, the innermost layer, the mucosa, was readily distinguished owing to its low reflectivity compared with the submucosa. Vascular structures were also identified within the wall (Fig. 2B). These high-resolution images demonstrate the capability of OCT to both resolve microstructural detail and image the entire rabbit esophagus to the serosa. In *in vivo* OCT images of the rabbit trachea permitted differentiation of the pseudostratified epithelium, mucosa, and surrounding hyaline cartilage (Fig. 3A). Because most neoplasms of both the esophagus and respiratory tract originate in the epithelium, the ability of OCT to precisely identify the mucosa could have important clinical implications.

A technology capable of performing optical biopsy should prove to be a powerful diagnostic modality in clinical medicine. Optical biopsy is defined here as imaging tissue microstructure at or near the level of histopathology without the need for tissue excision. At least three clinical scenarios exist in which optical biopsy will likely have a considerable impact on patient management. The first is in situations in which sampling errors severely restrict the effectiveness of excisional biopsy, such as the high failure rates associated with blind biopsies used to screen the premalignant conditions of ulcerative colitis or Barrett's esophagus (18). A need also exists for optical biopsy when conventional excisional biopsy is potentially hazardous. Examples of vulnerable regions include the central nervous

system, the vascular system, and articular cartilage. Finally, the ability to image at the cellular level could improve the effectiveness of many surgical and microsurgical procedures including coronary atherectomy, transurethral prostatectomies, and microvascular repair (8, 19, 20).

#### REFERENCES AND NOTES

- D. Huang *et al.*, *Science* **254**, 1178 (1991).
- A. F. Fercher, C. K. Hitzinger, W. Drexler, G. Kamp, H. Sattmann, *Am. J. Ophthalmol.* **116**, 113 (1993).
- E. A. Swanson *et al.*, *Opt. Lett.* **18**, 1864 (1993).
- M. R. Hee *et al.*, *Arch. Ophthalmol.* **113**, 325 (1995).
- C. A. Puliafito *et al.*, *Ophthalmology* **102**, 217 (1995).
- J. G. Fujimoto *et al.*, *Nature Med.* **1**, 970 (1995).
- J. M. Schmitt, A. Knuttel, M. Yadlowsky, M. A. Eckhaus, *Phys. Med. Biol.* **39**, 1705 (1994).
- M. E. Brezinski *et al.*, *Circulation* **93**, 1206 (1996).
- J. M. Schmitt, M. J. Yadlowsky, R. F. Bonner, *Dermatology* **191**, 93 (1995).
- G. J. Tearney *et al.*, *Am. J. Gastroenterol.*, in press.
- B. E. Bouma, G. J. Tearney, I. P. Bilinsky, B. Golubovic, J. G. Fujimoto, *Opt. Lett.* **21**, 1839 (1996).
- A. Seas, V. Petricevic, R. R. Alfano, *ibid.* **17**, 937 (1992).
- V. M. Gelikonov *et al.*, *JETP Lett.* **61**, 149 (1995).
- G. J. Tearney *et al.*, *Opt. Lett.* **21**, 1408 (1996).
- K. F. Kwong, D. Yankelevich, K. C. Chu, J. P. Heritage, A. Dienes, *ibid.* **18**, 558 (1993).
- J. P. Heritage, A. M. Weiner, R. N. Thurston, *ibid.* **10**, 609 (1985).
- G. J. Tearney *et al.*, *ibid.* **21**, 543 (1996).
- R. W. Phillips and R. K. H. Wong, *Gastroenterol. Clin. N. Am.* **20**, 791 (1991).
- G. J. Tearney *et al.*, *J. Urol.* **157**, 1913 (1997).
- M. E. Brezinski *et al.*, *J. Surg. Res.*, in press.
- The axial dimension of each OCT image was 2.3

mm, which was digitized to 248 pixels. Imaging could be performed with either 256 or 512 lateral pixels, corresponding to image acquisition times of 125 or 250 ms, respectively. All images were obtained with 512-pixel lateral resolution at four frames per second to optimize lateral sampling. The two-dimensional image data were displayed with a polar coordinate transformation and inverse gray scale. Data were recorded in both Super VHS and digital format.

- In vivo* imaging was performed on normal New Zealand White rabbits at 12 weeks of age. After the animals were anesthetized, the OCT imaging catheter-endoscope was introduced through a 2.3-mm guiding catheter into the gastrointestinal and respiratory tract. The respiratory tract was accessed directly through the trachea via a midline incision, and the gastrointestinal tract was entered through the oropharynx. Sites imaged included the oropharynx, esophagus, trachea, and bronchi (main, secondary, and tertiary). After imaging, the animals were killed and the imaged regions were excised and immersed in 10% formalin for routine histologic processing. The specimens were blocked in paraffin, cut into 5- $\mu\text{m}$  sections, and stained with hematoxylin and eosin (H&E) for microscopic examination.
- The contributions of E. A. Swanson (MIT Lincoln Laboratory) are greatly appreciated. We thank J. Gamba and J. Taralli for technical support and C. Kopf for help with preparation of the manuscript. Supported in part by NIH contract NIH-9-RO1-EY11289-10 (J.G.F.), the Medical Free Electron Laser Program, Office of Naval Research contract N00014-94-1-0717 (J.G.F.), the Air Force Office of Scientific Research contract F49620-95-1-0221 (J.G.F.), the Joint Services Electronics Program contract DAAH04-95-1-0038 (J.G.F.), the Whittaker Foundation contract 96-0205 (M.E.B.), and NIH contract NIH-1-R29-HL55686-01A1 (M.E.B.).

16 January 1997; accepted 10 April 1997

## Exchange of Protein Molecules Through Connections Between Higher Plant Plastids

Rainer H. Köhler, Jun Cao, Warren R. Zipfel, Watt W. Webb, Maureen R. Hanson\*

Individual plastids of vascular plants have generally been considered to be discrete autonomous entities that do not directly communicate with each other. However, in transgenic plants in which the plastid stroma was labeled with green fluorescent protein (GFP), thin tubular projections emanated from individual plastids and sometimes connected to other plastids. Flow of GFP between interconnected plastids could be observed when a single plastid or an interconnecting plastid tubule was photobleached and the loss of green fluorescence by both plastids was seen. These tubules allow the exchange of molecules within an interplastid communication system, which may facilitate the coordination of plastid activities.

Plastids are plant cell organelles that perform metabolic and biosynthetic reactions, including carbon fixation and synthesis of

fatty acids, carotenes, purines, and pyrimidines. Plastids contain multiple copies of a genome that encodes a subset of the organelle's RNA and protein molecules (1). Nuclear-encoded proteins are synthesized in the cytosol as precursors with transit peptides that target them to and across the chloroplast double-membrane envelope (2). Plastids are generally regarded as autonomous organelles that multiply by division and sort into daughter cells (1). We have

R. H. Köhler, J. Cao, M. R. Hanson, Section of Genetics and Development, Cornell University, Biotechnology Building, Ithaca, NY 14853-2703, USA.  
W. R. Zipfel and W. W. Webb, School of Applied and Engineering Physics, Cornell University, Ithaca, NY 14853-2703, USA.

\*To whom correspondence should be addressed. E-mail: mrh5@cornell.edu